Correspondence to:
A. S. Medvedev,
medvedev@mps.mpg.de

On the Dynamical Importance of Gravity Wave Sources Distributed Over Different Heights in the Atmosphere

Alexander S. Medvedev[1] , **Gary P. Klaassen[2]** , and **Erdal Yiğit[3]**

[1]Max Planck Institute for Solar System Research, Göttingen, Germany, [2]Department of Earth and Space Science and Engineering, York University, Toronto, ON, Canada, [3]Department of Physics and Astronomy, George Mason University, Fairfax, VA, USA

Abstract Gravity waves (GWs) are generated at all altitudes in the atmosphere, but sources above the lower stratosphere are rarely considered by parameterizations employed in general circulation models. This study assesses the potential impact on the thermosphere produced by small-scale waves originating at different heights. Within the proposed numerical framework, GW sources are represented by wave momentum forcing, whose values are expressed relative to the forcing required to obtain typical wave spectra around the tropopause. The relative importance of tropospheric and extra-tropospheric sources and the response in the thermosphere are studied in a series of sensitivity experiments. They demonstrate that the accumulation of wave momentum steeply drops with height as a consequence of decreasing density, even when the forcing is maintained at a uniform level throughout the middle atmosphere. When a broad spectrum is forced at twice the tropospheric rate, the thermospheric drag is increased by only a factor of two, and that increase is produced by waves that were forced in the lower stratosphere. With increasing altitude, vertically localized sources contribute progressively less. For example, for GWs excited near the mesopause to produce an impact comparable with that due to waves propagating from below, the forcing must be orders of magnitude stronger than in the troposphere. The estimated forcing of the so-called secondary harmonics by breaking primary waves is much weaker, such that the systematic dynamical effect of secondary waves in the thermosphere is negligible compared to that of the primary GWs generated in the troposphere.

Plain Language Summary Multiple observations demonstrate that gravity waves (GWs) are generated at all atmospheric levels, however numerical general circulation models employing parameterizations that account for wave sources only in the troposphere are able to reproduce the state and dynamics of the middle and upper atmosphere reasonably well. Assessing the role of GWs generated above the troposphere is extremely challenging, because such waves are difficult to separate from those of tropospheric origin in observations. The mechanisms of wave generation in the middle atmosphere are very complex and not fully understood. We developed a numerical framework, in which the strength of the extra-tropospheric sources is represented by multiples of those in the troposphere. In the series of sensitivity tests, we demonstrate that the contribution of sources to the total wave momentum drops with height following the density decrease, and that the tropospheric sources capture the major part of the total momentum and of the associated GW drag in the thermosphere. One of the conclusions of this study is that the impact in the thermosphere of secondary waves, which are believed to be excited near the mesopause, is negligible compared to that of primary waves propagating from the troposphere.

1. Introduction

Gravity waves (GWs) are ubiquitous at all altitudes, and are known for their ability to propagate vertically and dynamically couple atmospheric layers. They are a fundamental phenomenon in all convectively stable planetary atmospheres (Yiğit & Medvedev, 2019). GWs originating in lower and denser levels transport energy and momentum upward and provide strong impact on the dynamical and thermal structure of the upper atmosphere. The most recent reviews of the role of GWs in the vertical coupling in the atmospheres of Earth and other planets can be found in the works by Medvedev and Yiğit (2019) and Yiğit and Medvedev (2015), correspondingly. GWs are generated by a variety of sources, the most common of which are flow over topography, convection, instability, and transience of weather phenomena, and of the dynamics in general. There is growing observational evidence for GWs excited in the mesosphere (e.g., Heale et al., 2022; Kogure et al., 2020; Miao et al., 2022, and references therein). They are often called "secondary", because they are related to disturbances induced by

Writing – review & editing: Alexander S. Medvedev, Gary P. Klaassen, Erdal Yiğit

breaking "primary" harmonics arriving from below (Chun & Kim, 2008; Heale et al., 2020; Vadas et al., 2018). A strong thermospheric variability is associated with GWs generated by energetic particle precipitation, Joule heating, and variations of the equatorial electrojet (e.g., Williams, 1989; Yiğit, Medvedev, et al., 2012; Yiğit, Ridley, & Moldwin, 2012).

A necessary condition for vertical group propagation of GWs in a stratified fluid is the vertical displacement of air parcels. Being intrinsically dynamic and constantly changing, the atmosphere provides many opportunities for GWs to arise. There is no reason to believe that GW sources are limited to certain altitude regions or to a few physical mechanisms: in principle waves may be generated at any height where the stratification is stable. This assumption not only motivates the search for and investigation of such sources, but also raises the question of their importance. Almost all general circulation models (GCMs) utilizing parameterizations of subgrid-scale GWs place the sources in the troposphere or in the lowermost stratosphere. One exception known to us is the study of Ribstein et al. (2022), who imposed sources at all altitudes. How then can parameterizations ignoring sources in the rest of the atmosphere reproduce the observed large-scale circulations? Have the tropospheric sources been tuned to compensate for missing extra-tropospheric sources?

Our paper addresses these and related questions, and focuses on estimating the dynamical importance of (not yet specified) sources distributed at all heights. We define the importance of waves based on their (a) amplitudes (or fluxes) and (b) dynamical impact. The former is quantified in terms of the momentum flux carried by GWs, and the latter is expressed in terms of the produced momentum deposition, or "wave drag." We compare these quantities with the effects caused in the thermosphere by waves originating at lower altitudes. It should be noted that certain events can cause an enhanced generation at high altitudes, such that the locally induced GW activity exceeds the variance associated with harmonics arriving from below. Traveling ionospheric disturbances, which represent wave packets originating in the thermosphere, are well-known (Otsuka, 2021). These, however, are not the subject of our study. Instead, we focus on persistent effects of GWs, that is, those that systematically affect large-scale dynamics.

In Section 2, we introduce a theoretical framework describing evolution of the GW momentum flux with height, in which sources are introduced in terms of a specified body force. In order to provide a baseline for extra-tropospheric forcing, the magnitude of the body force required to produce typical GW spectra at altitudes just above the tropopause is estimated in Section 3. Sensitivity calculations demonstrating the response in the upper atmosphere to magnitudes and location of vertically distributed sources are presented next for sequentially more realistic cases. In Section 4, we assume sources are continuously distributed in altitude and consider the propagation of a single harmonic in a windless atmosphere. Next, the influence of the wind on that single harmonic and then separately on a spectrum of waves is explored. In Section 5, we consider vertically localized sources. Finally, in order to assess theories of secondary GW generation, we consider in Section 6 the impact of the variations of the horizontal wavelength of GWs excited near the mesopause. Discussion is presented in Section 7, and conclusions are given in Section 8.

2. Theory

We start with physical assumptions simplifying governing equations for GW dynamics, and which are consistent with many GW parameterizations employed in GCMs. They include (a) propagation in a two-dimensional frame and (b) assumption of incompressible hydrostatic nonrotating mid-frequency waves. The corresponding set of linearized equations has a form similar to Holton (2004, Equations 7.37–7.40):

$$\frac{du'}{dt} + \frac{1}{\rho_0}\frac{\partial p'}{\partial x} = 0, \tag{1}$$

$$\frac{1}{\rho_0}\frac{\partial p'}{\partial z} - \frac{\theta'}{\bar{\theta}}g = 0, \tag{2}$$

$$\frac{d\theta'}{dt} + w'\frac{d\bar{\theta}}{dz} = 0, \tag{3}$$

$$\frac{\partial u'}{\partial x} + \frac{\partial w'}{\partial z} = 0, \tag{4}$$

where u', w', p', and θ' are the wave-induced disturbances of the horizontal and vertical wind, pressure, and potential temperature, correspondingly, $\rho_0(z)$ is the background density, g is the acceleration of gravity, $d/dt = \partial/\partial t + \bar{u}\partial/\partial x$ is the material derivative and the bar over a variable indicates an appropriate averaging. Exclusion of θ' from Equations 2 and 3 yields

$$\frac{1}{\rho_0}\frac{d}{dt}\frac{dp'}{dz} + N^2 w' = 0, \tag{5}$$

where

$$N^2 = \frac{g}{\bar{\theta}}\frac{d\bar{\theta}}{dz} \tag{6}$$

is the squared Brunt-Väisälä (or buoyancy) frequency. Equation 5 together with the equations of momentum conservation (Equation 1) and continuity (Equations 4) represent a closed set of equations for u, w, and p.

Waves can be excited by applying forcing to any field variable. Without loss of generality, we can assume that they are generated by a horizontal momentum force (per unit mass) $\mathcal{G}(x, z, t)$, the precise form of which is not specified at this point. Since Equation 2 is hydrostatic, the continuity Equation 4 imposes corresponding oscillatory vertical motions. The linearity of the equations allows for representing all wave variables ψ as the sum of Fourier harmonics

$$\psi' = \sum_j \psi_j(z)\exp\left[i(\omega_j t - k_j x)\right], \tag{7}$$

where ψ_j is the complex amplitude, k is the horizontal wavenumber, which we assign to be positive; ω is the observed frequency that can have either sign, and the index j notates pairs of (ω, k), thus formally converting the summation over two indices to a single sum. Then the set of algebraic equations corresponding to Equations 1, 4, and 5 has the form

$$i\hat{\omega}_j u_j + w_j \bar{u}_z - ik_j \rho_0^{-1} p_j = -G_j, \tag{8}$$

$$\frac{i\hat{\omega}_j}{\rho_0}\frac{dp_j}{dz} + N^2 w_j = 0, \tag{9}$$

$$-ik_j u_j + \frac{dw_j}{dz} = 0, \tag{10}$$

where we have introduced the intrinsic frequency $\hat{\omega}_j = \omega_j - k_j \bar{u}$. In Equations 8–10, u_j, w_j, p_j, and G_j are the (complex) Fourier amplitudes of the wave-induced disturbances of the horizontal and vertical wind, pressure, and momentum force $\mathcal{G}$, correspondingly; the subscripts j indicate they are all functions of the horizontal wavenumber k_j and observed frequency ω_j, while the subscript z (e.g., $\bar{u}_z$) denotes a vertical gradient. In the rest of this section, we omit the subscripts j for simplicity.

Eliminating p (i.e., p_j) from Equations 8 and 9, we obtain

$$\left[\frac{N^2 k^2}{\hat{\omega}^2} - \frac{1}{\hat{\omega}\rho_0}\frac{d}{dz}(\rho_0 \hat{\omega}_z)\right]w + iku\left(\frac{\hat{\omega}_z}{\hat{\omega}} + \frac{\rho_{0z}}{\rho_0}\right) + ik\frac{du}{dz} - \frac{\hat{\omega}_z}{\hat{\omega}}\frac{dw}{dz} = -\frac{k}{\hat{\omega}\rho_0}\frac{d(\rho_0 G)}{dz}. \tag{11}$$

Substitution of Equation 10 into Equation 11 yields the equation for the vertical structure

$$\frac{d^2 w}{dz^2} + \frac{dw}{dz}\frac{\rho_{0z}}{\rho_0} + w\left[\frac{N^2 k^2}{\hat{\omega}^2} - \frac{1}{\rho_0 \hat{\omega}}\frac{d}{dz}(\rho_0 \hat{\omega}_z)\right] = -\frac{k}{\rho_0 \hat{\omega}}\frac{d}{dz}(\rho_0 G). \tag{12}$$

Equation 12 describes the vertical propagation of the GW harmonic (ω, k) forced by the corresponding spectral component of the source term in the right-hand part. It can be converted to a more familiar Taylor-Goldstein form by introducing the new variable $W = w\exp\left[+1/2\int(\rho_{0z}/\rho_0)dz'\right]$ and eliminating the term containing the first derivative.

A general solution of Equation 12 can be sought in the form

$$w \propto \exp\left(i \int_{z_s}^{z} m(z') dz' \right), \tag{13}$$

where m is the complex local vertical wavenumber $m = m_R - im_I$. Note that $m_R > 0$, if only upward propagating harmonics are considered. The expressions for m_R and m_I can be obtained by substituting Equation 13 into the equation for freely propagating waves, that is, in Equation 12 with the forcing term $G = 0$:

$$m_R^2 = \frac{N^2 k^2}{\hat{\omega}^2} - \frac{1}{4}\left(\frac{\rho_{0z}}{\rho_0} \right)^2, \qquad m_I = -\frac{\rho_{0z}}{2\rho_0} + \frac{\hat{\omega}_z}{2\hat{\omega}}. \tag{14}$$

In the derivation of Equation 14, we assumed that (a) the atmosphere has strong stratification $\left(N^2/\bar{u}_z^2 > 1 \right)$ and (b) the background wind varies with height sufficiently slowly such that $\bar{u}_{zz}$ tends to zero (Jones, 1967). The terms $m_I^2 + m_I \rho_{0z}/\rho_0 + dm_I/dz$ were neglected with respect to m_R^2. The second term $(\rho_{0z}/2\rho_0)^2 = 1/4H^2$ in the expression for m_R can further be neglected with respect to the first one under the assumption of short vertical wavelengths $2|m|H \gg 1$, which has been made previously by adopting Equations 1–4.

The analysis can be easily extended to account for wave dissipation/damping by replacing $\hat{\omega} \to \hat{\omega} - id_R$, where d_R is the damping coefficient, whose particular form depends on the mechanism. Then Equation 14 takes the form

$$m_R^2 = \frac{N^2 k^2}{\hat{\omega}^2}, \qquad m_I = -\frac{\rho_{0z}}{2\rho_0} + \frac{\hat{\omega}_z}{2\hat{\omega}} - \beta, \tag{15}$$

where β is the vertical damping rate. A discussion and parameterizations of β for main dissipation mechanisms affecting GWs in the atmosphere can be found in the work by Yiğit et al. (2008, Section 3).

The next step is to obtain an equation for the squared amplitude, which is a purely real quantity. For this, we multiply Equation 11 by the complex conjugated u^*, and add the complex conjugated Equation 11 multiplied by u. Based on Equation 13, we represent Equation 10 in the form $ku = mw$ for replacing terms with w in Equation 11. Using the explicit expressions (Equation 15) for m_R and m_I, we obtain

$$\frac{d|u|^2}{dz} = \left(-\frac{\rho_{0z}}{\rho_0} + \frac{m_z}{m} - 2\beta \right)|u|^2 + \frac{2}{\hat{\omega}\rho_0}|u|\frac{d\rho_0|G|}{dz}\sin\phi. \tag{16}$$

In Equation 16, $|u|^2 = uu^*$ is the squared amplitude of the wave-induced horizontal wind fluctuations, and ϕ is the phase shift between the oscillations of u and G. Note that the wave phase is understood, as defined in Equation 7. The forcing term in the right-hand part maximizes, if the oscillations of u and G are shifted by $\pi/2$. If they are in- or opposite phase, the net forcing is zero. Then the remaining equation collapses to the known one (e.g., Medvedev & Klaassen, 1995, Equation 10), which describes the evolution of the wave amplitude with height under the influence of density stratification, refraction by the mean wind and dissipation/breaking, correspondingly. In such form, it is used in the parameterization for GCMs (Medvedev & Klaassen, 2000, Equation 1).

We proceed further to obtain a more compact form and re-write (Equation 16) for the vertical flux of horizontal momentum (momentum flux, for brevity) $F_M = \text{Re}(uw)$ by substituting the relation $|u|^2 = m_R F_M/k$ into Equation 16

$$\frac{dF_M}{dz} = \left(-\frac{\rho_{0z}}{\rho_0} - 2\beta \right)F_M + \frac{2}{N}\sqrt{\frac{m_R}{k}}\sqrt{F_M}\frac{d(\rho_0|G|)}{\rho_0 dz}\sin\phi. \tag{17}$$

It describes how the wave momentum flux changes with height in the presence of both wave damping β and forcing G. If $(\beta = G = 0)$, the total momentum flux $\rho_0 F_M$ associated with the propagating harmonic is conserved. If $G = 0$ and $\beta \neq 0$, Equation 17 converges to Equation 25.1 in the paper by Yiğit & Medvedev (2013). Thus, Equation 17 represents an extension of the spectral nonlinear scheme of Yiğit et al. (2008) to include GW sources in the atmosphere in addition to their distribution at the lower boundary. Equation 17 is a Bernoulli-type ODE, the solution of which has the form (e.g., Polyanin & Zaitsev, 2017, Section 1.2.3)

$$F_M(z) = \frac{\rho_s}{\rho_0(z)}e^{-2\tau}\left[\sqrt{F_M(z_s)} + \int_{z_s}^{z}\frac{\sin\phi}{\sqrt{N\hat{\omega}}}\sqrt{\frac{\rho_0}{\rho_s}}\frac{d(\rho_0|G|)}{\rho_0 dz}e^{\tau}dz' \right]^2, \tag{18}$$
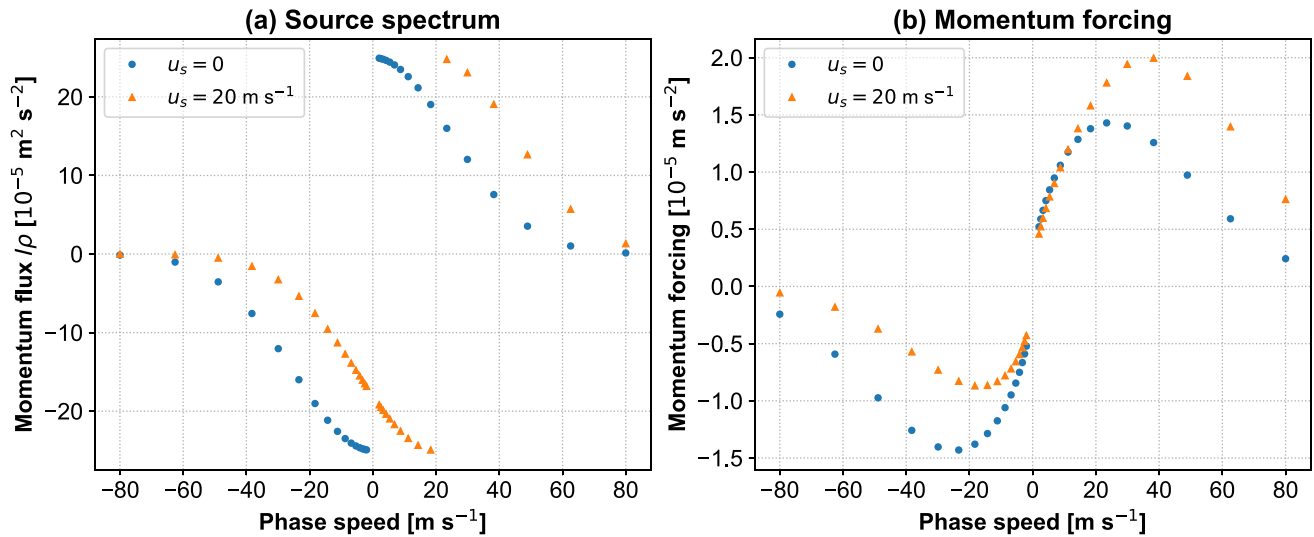
Figure 1. (a) The reference momentum flux (per unit mass) spectrum at the source level (in m^2 s^{-2}, Equation 19) and (b) estimated characteristic forcing $|G|$ (in m s^{-2}, from Equation 20) required for generating the reference spectrum at $z_s = 15$ km as functions of the observed phase speed of harmonics. Blue dots correspond to $\bar{u}_s = \bar{u}(z_s) = 0$ and orange triangles are for the representative background wind at the source level $\bar{u}_s = 20$ m s^{-1}.

where $F_M(z_s)$ and ρ_s are the momentum flux and mean density at the lower boundary z_s, correspondingly; the function $\tau(z) = \int_{z_s}^{z} \beta(z')dz'$ encapsulates all the damping mechanisms affecting the propagating harmonic (Yiğit et al., 2008, Equation 2). Without the forcing $G(z)$, Equation 18 yields a solution for F_M with the prescribed boundary condition $F_M(z_s)$ at the source level (cf. Yiğit et al., 2008, Equation 1). The second term in the square brackets describes the cumulative effect of wave sources located below the altitude of interest z.

3. Forcing Function

Before turning to applications of Equation 18, one has to consider how to constrain the forcing function $|G|\sin\phi$. Reiterating the definition from the previous section, $|G(z)|$ describes the amplitude of the horizontal momentum forcing (per unit mass) applied to the GW harmonic (ω, k) at a given height z, while $\phi(z)$ is the phase shift angle between the forcing and wave-induced disturbances of the horizontal velocity. Various mechanisms of wave generation, linear or nonlinear, can formally be described (parameterized) in terms of G, as has been done for the damping rate β. Developing parameterizations of G for particular physical processes is beyond the scope of this paper. Instead, we will focus on exploring the sensitivity of the solution (Equation 18) to hypothetical sources encompassed by various functions $G(z)$. In doing so, certain assumptions about G must be made. It is unlikely that various forcing processes in the atmosphere act always in sync with a harmonic originating in the troposphere and amplify it. This means that $\sin\phi$ can vary between -1 and 1, and the source term in Equation 18 can both add to or subtract from the momentum flux $F_M(z_s)$ associated with the harmonic. We will consider the most favorable condition for forcing by assuming that sources always contribute to the wave growth, that is, $\sin\phi = 1$. This means that the obtained results must be viewed as upper limit estimates of the importance of vertically distributed sources.

The next step is to evaluate a typical magnitude of the forcing term $|G|$ for the troposphere. For this, we turn to the results of GCM modeling. Multiple simulations using the spectral GW parameterization of Yiğit et al. (2008) have shown that the set of 32 harmonics j with observed phase speeds $c_j = \omega_j/k_j$ at the source level near the edge of the troposphere ($z_s = 15$ km) having fluxes (Yiğit, Medvedev, et al., 2012; Yiğit, Ridley, & Moldwin, 2012, Equation 1, Figure 1)

$$F_{Mj}(z_s) = \text{sgn}(c_j - \bar{u}_s)\overline{u'w'}_{\max}\exp\left[-(c_j - \bar{u}_s)^2/c_w^2\right] \tag{19}$$

provided the best match of the simulated circulation with observations. This was also confirmed by comparison with the results from the GW resolving model extending into the thermosphere (Miyoshi et al., 2014, Section 3.3). The distribution (Equation 19) provides a very good match with the balloon measurements in the upper

troposphere (Hertzog et al., 2008, Figure 6). In Equation 19, $\bar{u}_s = \bar{u}(z_s)$ is the background wind at the source level and c_w represents the half-width of the Gaussian spectrum, and we restored the index j. The spectrum was confined to $|c| \leq 80$ m s^{-1}, corresponding to an unshifted vertical wavelength of 25 km. Waves with significantly faster intrinsic horizontal group speeds and longer vertical wavelengths would violate the column model assumption as well as the incompressible approximation $mH \gg 1$. Moreover, not much is known about the statistics of internal waves in the middle atmosphere with vertical wavelengths on the order of the depth of the stratosphere.

It is plausible to believe that these harmonics were generated in the layers below the source level. If we assume that $|G_j|$ is constant with height, there is no wave damping ($\tau = 0$), there are no fluxes at the surface ($F_{Mj}(z = 0) = 0$), and that the troposphere is windless and isothermal ($T = 240$ K), then Equation 18 can be solved analytically:

$$F_{Mj}(z_s) = e^{\frac{z_s}{H}} \frac{4k|G_{\text{trop},j}|^2}{Nc_j} \left[e^{-\frac{z_s}{2H}} - 1 \right]^2. \tag{20}$$

In Equation 20, the integer index j marks individual harmonics of the spectrum having the phase velocity c_j. Equating F_{Mj} at $z = z_s$ to that from Equation 19 gives an estimate of the characteristic momentum forcing $|G_{\text{trop},j}|$ required for creating the distribution (Equation 19) at 15 km. The source spectrum and the characteristic $|G_{\text{trop},j}|$ are shown in Figure 1 as functions of observed phase velocities c_j. The parameters $\overline{u'w'}_{\max} = 2.5 \cdot 10^{-4}$ m^2 s^{-2}, $c_w = 35$ m s^{-1} and $k = 2\pi/(300$ km$)$ from Yiğit et al. (2009) were used along with $u_s = 0$. Numerical solution of Equation 18 for more realistic background conditions can be carried out, however here we note that those calculated G_j differ from the estimates in Figure 1 very little (by not more than 10%), especially for fast harmonics, whose phase speed exceeds the background wind in the troposphere.

4. Vertically Homogeneous Sources

4.1. Single Harmonic

Solution of Equation 18 for vertically varying mean wind and temperature can be obtained numerically. For that, we updated the scheme of Yiğit et al. (2008) to include the forcing term containing G. The vertical damping rates β due to the major breaking/dissipation processes affecting GWs in the atmosphere (nonlinear wave-wave interactions, molecular diffusion and thermal conduction, and ion friction) were accounted for as described in Yiğit et al. (2008, Section 3). We provide the explicit expressions for the latter two, because they will be required in the course of the paper

$$\beta_{mol} = \frac{\nu_{\text{mol}} N^3}{k\hat{c}^4}, \qquad \beta_{ion} = \frac{\nu_{\text{ni}} N}{k\hat{c}^2}, \tag{21}$$

where ν_{mol} is the molecular viscosity and ν_{ni} is the neutral-ion collisional frequency. The momentum lost by a harmonic and transferred to the mean flow (or, alternatively, "wave drag") can be found as follows:

$$a = \frac{1}{\rho_0} \frac{d(\rho_0 F_M)}{dz}. \tag{22}$$

In order to explore the mechanics of how vertically distributed sources affect the solution, we performed calculations for the simplest case of a single harmonic subject to forcing that remains constant with altitude. We neglect the mean wind $\bar{u}$, but account for vertically varying mean temperature. A harmonic with $k = 2\pi/(300$ km$)$ and $c = 80$ m s^{-1} was selected from the spectrum (Equation 19) as having the largest vertical wavelength and, thus, less affected by molecular diffusion and critical level filtering and, therefore, having a better chance to penetrate higher. Note that the harmonic still was able to interact nonlinearly with itself, as was described in detail in the papers of Medvedev and Klaassen (2000, Section 7) and Yiğit et al. (2008, Section 5). The background temperature profile was taken from the NRLMSIS00 model, and corresponds to the noon of 15 June 2000 at 45°N. The launch height was $z_s = 15$ km. Vertical profiles of the molecular viscosity coefficient and neutral-ion frequency for calculating ion friction are given in the paper of Yiğit and Medvedev (2010, Figure 1).

Two factors in Equation 18 affect the shape and vertical extent of the momentum flux profile: the cumulative factor associated with the additional (to $F_M(z_s)$) supply from the distributed sources (the term in the square brackets) and the damping factor $\exp(-2\tau)$, which varies between 0 and 1 and can alternatively be viewed as a transmissivity. They are plotted in Figure 2a with solid and dotted lines, respectively. The factor ρ_s/ρ_0 simply reflects
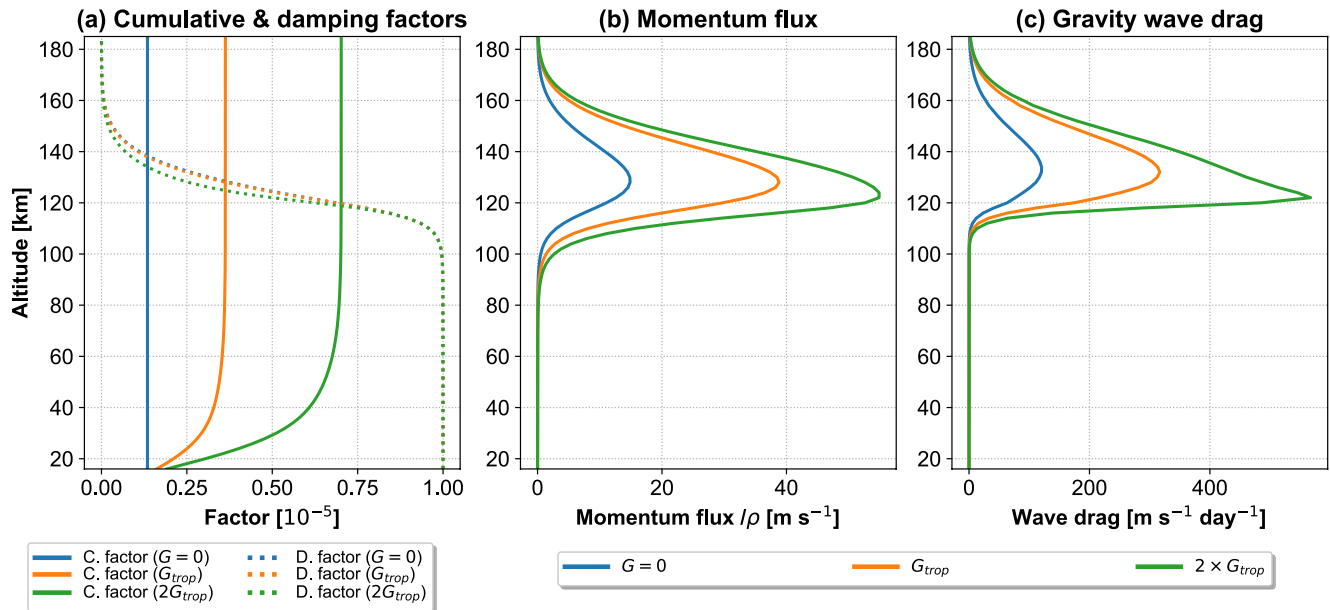
Figure 2. (a) Cumulative and damping (transmissivity) factors, (b) momentum flux (per unit mass), and (c) produced gravity wave drag calculated for the harmonic with the phase velocity $c = 80$ m s^{-1} in the absence of the mean wind ($\bar{u} = 0$). Blue line is for the absence of generation above the source level ($G = 0$), orange line is for the same magnitude of sources below and above the launch height ($G = G_{\text{trop}}$), and green line is for doubled forcing above the source level ($G = 2 \times G_{\text{trop}}$). The other information is given in the caption and text.

the exponential growth of the momentum flux per unit mass with height. Without additional sources ($G = 0$, blue lines), the profiles correspond to the original parameterization of Yiğit et al. (2008). Accordingly, the cumulative factor remains constant with height and equal to the source value $F_M(z_s)$. It is seen that the damping is negligible up to ~100 km, and then continuously increases with height. The resulting profiles of F_M and drag are plotted in Figures 2b and 2c, correspondingly.

In the next two examples, we assume that the effectiveness of wave generation above the source level is the same as in the troposphere ($G = G_{\text{trop}}$, orange lines) and even twice larger ($G = 2 \times G_{\text{trop}}$, green). It is seen that the cumulative factors steeply grow with height at lower levels and cease the growth at higher altitudes above the stratopause. Upon saturation, they reach ~2.7 and 5.2 times of $F_M(z_s)$, correspondingly. The damping factors in the $G = 0$ and $G = G_{\text{trop}}$ calculations are almost indistinguishable. This means that the wave dissipation depends little on the flux magnitude, and occurs mainly due to molecular diffusion, whose damping rate is determined by the characteristics of the harmonic, namely by the horizontal wavelength and the intrinsic phase speed. When wave generation in the atmosphere is strong ($G = 2 \times G_{\text{trop}}$), the amplitude of the harmonic becomes sufficiently large to trigger nonlinear breaking/dissipation, and the transmissivity drops somewhat more steeply with height. Consequently, the peaks of the momentum flux and drag shift lower. The magnitudes of both increase approximately to the same degree as the cumulative factor.

A somewhat more realistic case that accounts for the background wind is presented in Figure 3. It demonstrates that the refractive properties of $\bar{u}$ can significantly modify the propagation of even fast harmonics, those which avoid filtering in the middle atmosphere. Wave damping onsets lower than in Figure 2 (below 100 km), approximately coinciding with the location of the maximum of the westerly jet (see Figure 4a). The latter shrinks the intrinsic phase speed $\hat{c}$ and shifts the local vertical wavenumber m to larger values, thus making the harmonic more susceptible to diffusion. Above ~115 km, the wind changes sign, $\hat{c}$ increases compared to the windless case, and the harmonic experiences less damping. It penetrates higher into the thermosphere before obliteration by molecular diffusion and deposits more drag there. The background wind enters the cumulative factor in Equation 18 associated with the additional sources through the intrinsic frequency $\hat{\omega}$. Comparison of Figures 2 and 3 shows that the cumulative factors remain virtually unchanged with the addition of the wind. Contrary to that, most of the dependence on the wind is encapsulated in the damping/transmissivity factor $\exp(-2\tau)$. It results in different vertical profiles of F_M and drag and of their peak values. However, the ratios between the cases with $G = 0$, $G = G_{\text{trop}}$ and $G = 2 \times G_{\text{trop}}$ remain approximately same as in the windless calculations at all altitudes. It should be mentioned
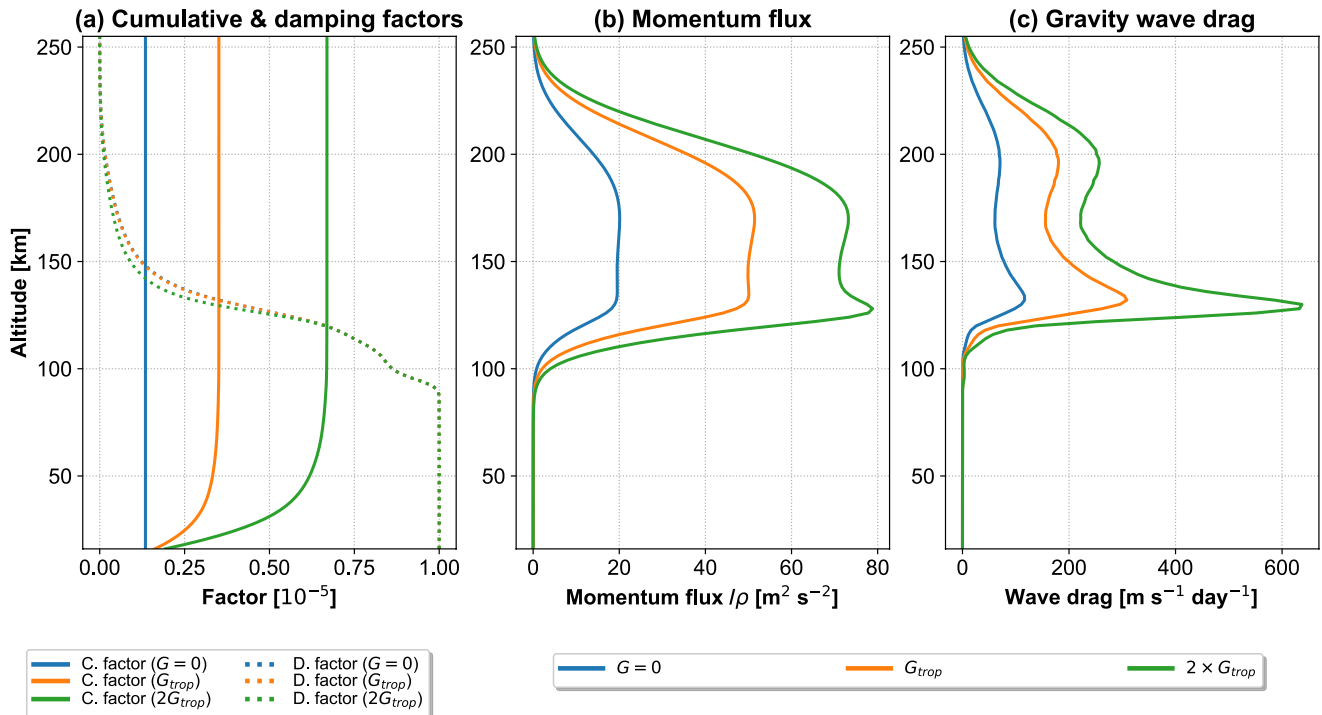
Figure 3. The same as in Figure 2, but with the mean wind $\bar{u}$ shown in Figure 4.

that although the two cases in Figures 2 and 3 show substantial increases in thermospheric drag under the influence of stronger forcing, it is for a single fast harmonic that is not strongly damped in the thermosphere. Moreover, that single harmonic is propagating in isolation, while sources often produce multiple harmonics propagating in opposite directions. As will be demonstrated in the next section, the thermospheric drag is greatly reduced when the wave spectrum includes a broad range of phase speeds propagating in both positive and negative azimuths.
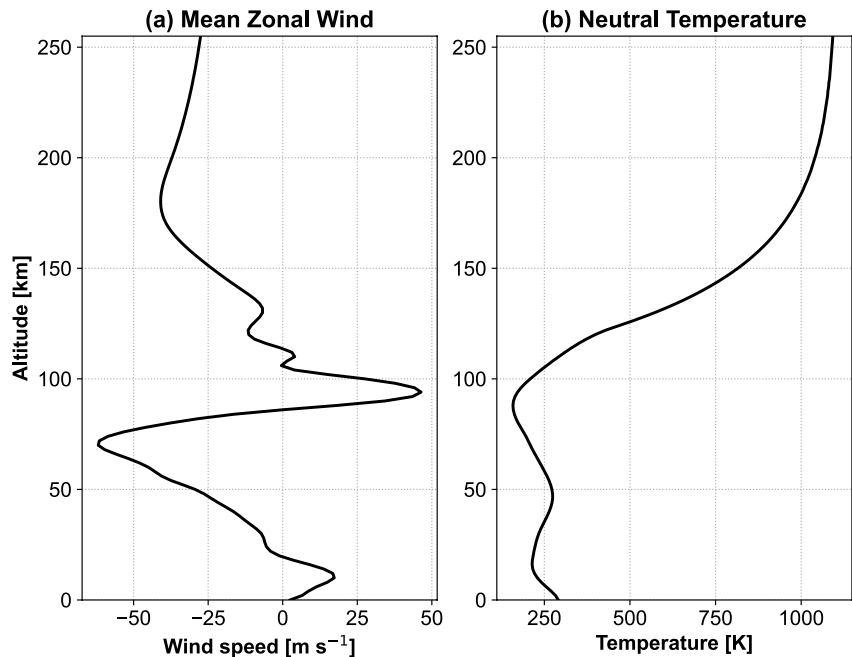

Figure 4. (a) Mean zonal wind $\bar{u}$ and temperature $\bar{T}$ at 45°N for 15 June 2000, 12:00 UT used in the calculations. The profiles are taken from the Horizontal Wind Model 2014 (HWM14) and NRLMSIS00 models.
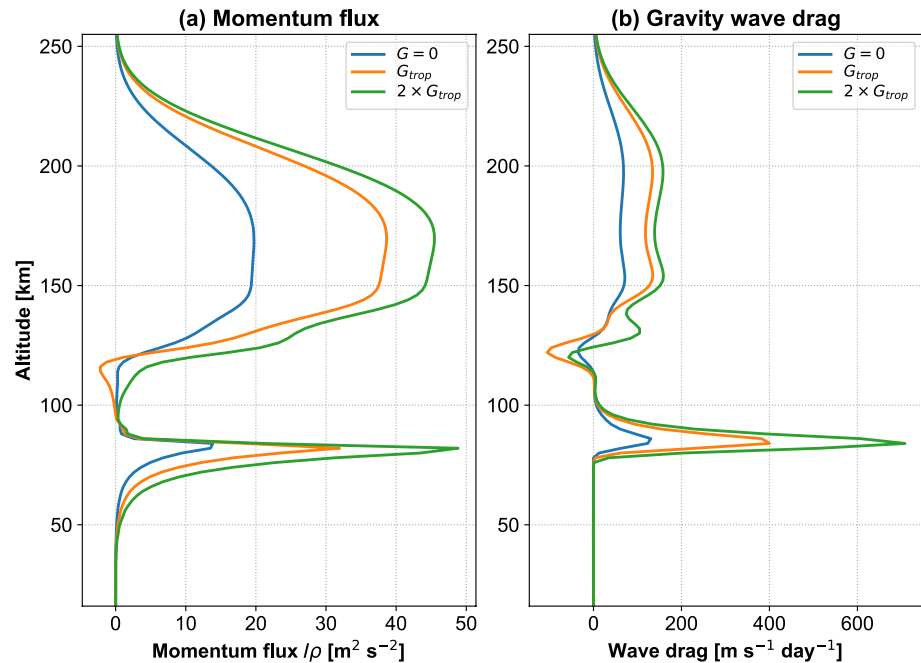
Figure 5. (a) Momentum flux F_M and (b) gravity wave drag calculated for the incident broad spectrum in Figure 1a. Blue lines are for the basic scenario without additional source ($G = 0$); orange lines are for the same sources above and below the launch height ($G = G_{\text{trop}}$); green lines are for the case of the double magnitude of sources ($G = 2 \times G_{\text{trop}}$).

4.2. Broad Spectrum

We next turn to a more general case and consider propagation of a broad spectrum of waves shown in Figure 1a. The characteristic forcing in the troposphere $|G_{\text{trop},j}|$ required for achieving the prescribed amplitudes at the source level was calculated for each harmonic j using Equation 20 and is plotted in Figure 1b. We compare in Figure 5 the basic scenario of no additional sources ($G_j = 0$, blue lines) with $G_j(z) = G_{\text{trop},j}$ (orange) and $G_j(z) = 2 \times G_{\text{trop},j}$ (green) applied to each harmonic. The majority of the harmonics from the incident spectrum are filtered out by the mean wind before reaching the thermosphere. Those with $\hat{c} < 0$ are obliterated by the westward wind relatively low, where their amplitudes were small. The other harmonics with $\hat{c} > 0$ propagate higher, but eventually dissipate too forming strong maxima of F_M and GW drag near the mesopause. An inspection of Figure 5 shows that the momentum flux in the mesosphere scales approximately as 1:2:3 between the presented scenarios. This means that the sources above the launch altitude contribute about the same momentum as G_{trop} generated in the troposphere. Note that this altitude range is where the cumulative factors grow steeply with height.

In the thermosphere, the wave activity and drag are mainly associated with a few fast harmonics that survived critical level filtering. Although the slower harmonics that have been filtered by critical levels continue to be forced above those levels, they do not reach amplitudes that are large enough to have a major impact in the thermosphere. In the present case, these fast harmonics are directed both along and against the mean wind, hence the momentum flux and GW drag shown in Figure 5 represent vector sums of the contributions of these harmonics. A partial cancellation due to Doppler shifting associated with the mean wind explains why F_M and the drag are smaller than the corresponding values for a single harmonic in Figure 3. Without the mean wind, the cancellation is full, and no net flux and drag is produced. An additional factor (to molecular diffusion which dominates in the thermosphere) that limits amplitudes is the nonlinear vertical damping β_{non}^j, which accounts for the presence of other harmonics and depends on the amplitude of those with shorter vertical wavelength and slower phase speeds. Overall, while imposing sources above the troposphere ($G = G_{\text{trop}}$) approximately doubles the GW response in the thermosphere, their further increase ($G = 2 \times G_{\text{trop}}$) does not produce a proportional response.

Additional tests were carried out for the wind and temperature profiles corresponding to 15 January 2000 00UT. In this case, the middle atmosphere jet is reversed compared to Figure 4 owing to the change of season. The thermospheric wind is also different owing to intraday variations. While details of the drag distribution are affected,
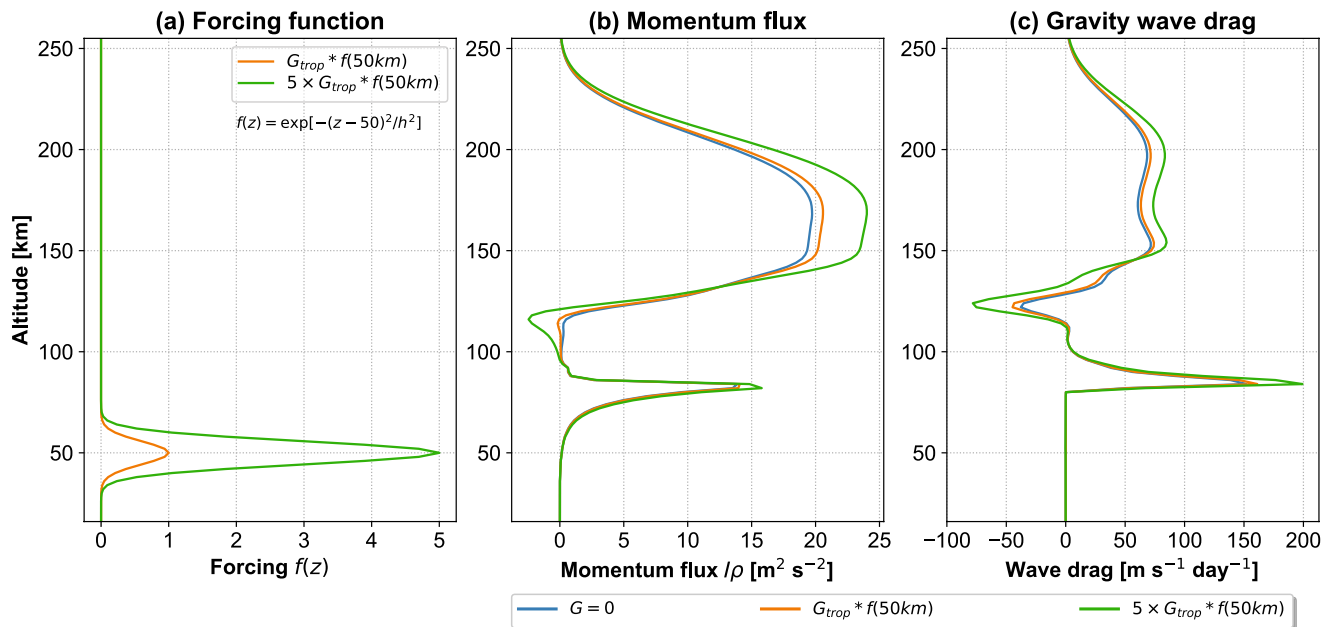
Figure 6. Calculations for the vertically localized source centered around 50 km (panel (a)) for two peak values: G_{trop} (orange) and $5 \times G_{\text{trop}}$ (green); (b) momentum flux F_M; (c) gravity wave drag. The calculations without sources are shown in blue.

the 15 January profile does not change the overall magnitude of the drag, therefore the results are not shown here. For example, since sources have both eastward and westward components, critical level dissipation of waves will produce net drag mainly opposite to the direction of the local mean wind, but with roughly the same magnitude as in the opposite season. Similarly, Doppler shifting of the vertical wavelength affects wave dissipation in the upper atmosphere. The drag changes direction according to the wave azimuth, but the magnitude of the drag is not drastically altered. Thus, the single profile in Figure 4 produces sufficiently general results regarding the overall effects of middle atmosphere wave sources.

5. Vertically Localized Sources

After estimating gross possible effect of wave sources distributed in the entire atmosphere, we consider localized ones by assuming a Gaussian distribution $|G(z)| \propto f(z) = \exp\left[-(z - z_m)^2/h^2\right]$, where z_m is the altitude of the peak, and h is the half-width, or vertical extent of the source region. In the calculations presented in this section, h was equal to the scale height at the peak, or ~ 8 km. The results for the source centered near the stratopause around $z_m = 50$ km, a layer in which primary waves experience dissipation by critical levels, are shown in Figure 6. It illustrates the response to two characteristic magnitudes: the one equal to the tropospheric forcing $G = G_{\text{trop}}f(z)$ (orange lines) and the one five times stronger $G = 5 \times G_{\text{trop}}f(z)$ (green). It is seen that the former source produces little difference to the momentum flux and GW drag profiles (Figures 6b and 6c) compared to the scenario without the imposed source (blue lines). The latter (stronger) forcing magnifies them by up to 10%–20% in the thermosphere. The reason for much weaker impact of the localized sources compared to the vertically homogeneous ones is the much smaller accumulation of injected momentum. This effect is quantified by the cumulative factor in Equation 18.

In the second experiment, the source was centered at 90 km, that is, at or just above the region of local maximum of wave breaking/saturation and GW drag in the mesosphere. The response in the thermosphere for the source strength presented in the figures above was extremely small and almost indistinguishable. Instead we plotted in Figure 7 the results for the forcing amplitude one and two orders of magnitude larger than the characteristic strength in the troposphere, that is, $G = 10 \times G_{\text{trop}}$ (orange lines) and $G = 100 \times G_{\text{trop}}$ (green), correspondingly. It is seen that even in the latter case, the momentum flux and GW drag increase by only about one third. This result is physically obvious and mathematically captured by the cumulative term: the air in the mesosphere is very thin, and in order to produce a noticeable change in the thermosphere, sources there must be unusually strong compared to the troposphere.
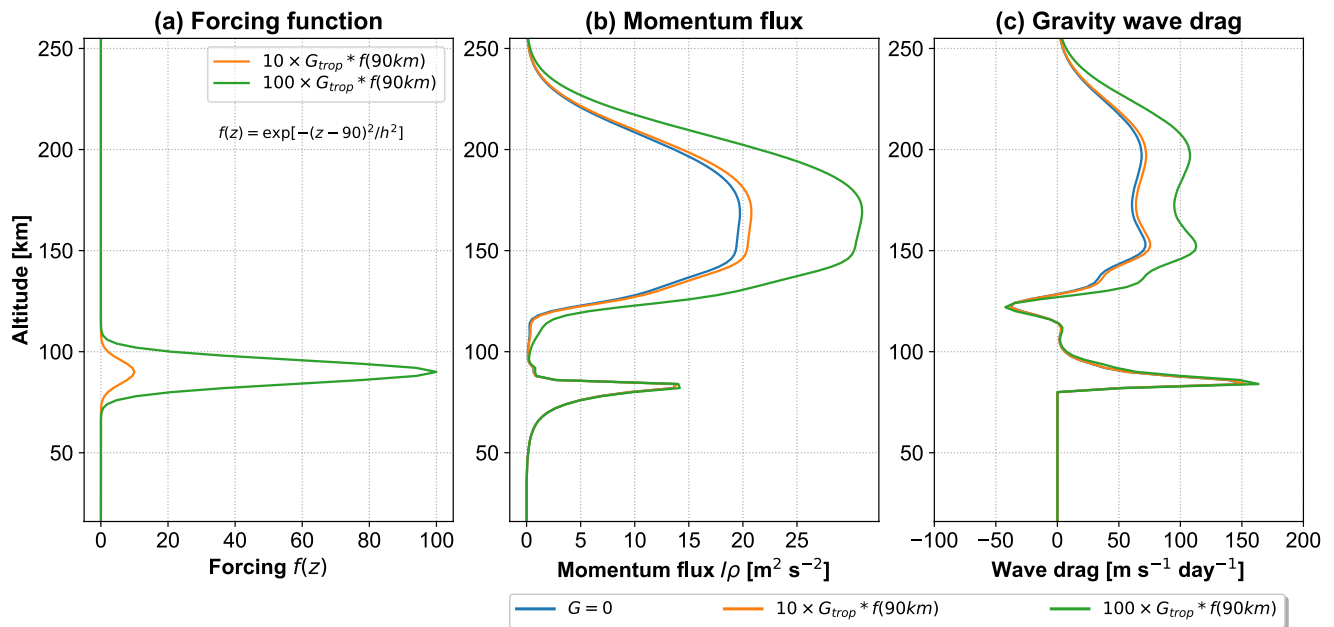
Figure 7. The same as in Figure 6, but for the sources centered around 90 km. Orange lines are for the peak values $G(90\text{ km}) = 10 \times G_{\text{trop}}$ and green lines are for $G(90\text{ km}) = 100 \times G_{\text{trop}}$. The calculations without sources are shown in blue.

6. Secondary Wave Sources

The mesosphere and lower thermosphere and the mesopause region, in particular, is a dynamically active atmospheric layer, which is continually disturbed by tides, space weather, sudden stratospheric warmings and also by transient and breaking GW packets arriving from below. Obviously, any of these processes can facilitate enhanced wave generation. Here we will focus on two proposed mechanisms for such "secondary" (in currently accepted terms) harmonics. One description is based on intermittency of localized body forces induced by breaking "primary" harmonics (Vadas & Fritts, 2002; Vadas et al., 2003). A different approach emphasizes nonlinear effects within wave packets, whose components achieve large amplitudes before breaking (Fritts et al., 2020, 2015). It is quite possible that the latter theory represents a nonlinear extension of the former approach (Fritts et al., 2022), or that both describe different phases of wave packet evolution. Regardless of whether the secondary waves are triggered by the turbulent collapse of primary wave packets or nonlinearly transformed from primary harmonics, both mechanisms predict secondary wave scales should be different from those of the primary waves. Specifically, the body force theory underscores the importance of longer horizontal wavelengths, attributing the maximum momentum flux to the secondary harmonic having twice the horizontal wavelength of the primary, while the nonlinear approach implies the momentum flux is transferred to shorter secondary harmonics.

The potential impact of these two secondary wave generation mechanisms on the thermosphere can be investigated in the current framework by changing the characteristic horizontal wavelength of a localized source placed at 90 km altitude. In order to isolate the effects of high-altitude sources, we exclude primary waves altogether by assigning $F_M(z_s)$ in Equation 18 to zero. The calculations in Figure 8 have been performed for the same localized Gaussian source distribution $f(z)$ and the same phase speed distribution as in Figure 7. Although this excludes fast components with $|c| > 80$ m s^{-1} originating in the troposphere, the results with and without tropospheric sources can then be directly compared. Two important but admittedly uncertain parameters have to be specified for performing the sensitivity tests: the intensity of the sources (the wave forcing G) and the characteristic horizontal wavelength ($\lambda_H = 2\pi/k$). For the first, we explore the parameter space in multiples of G_{trop}, as in the previous section. To cover both the body force and nonlinear cases, we assume that horizontal wavelengths of the excited waves are either three times longer or shorter than in Figure 7. We note that decreasing the horizontal wavelength significantly below 100 km can lead to violation of the hydrostatic approximation employed in this study, since m for faster harmonics tends to approach k.

The calculated profiles of momentum fluxes F_M and GW drag are plotted in Figure 8. First, we consider the dependence on the source strength keeping the same characteristic horizontal wavelength as in previous sections
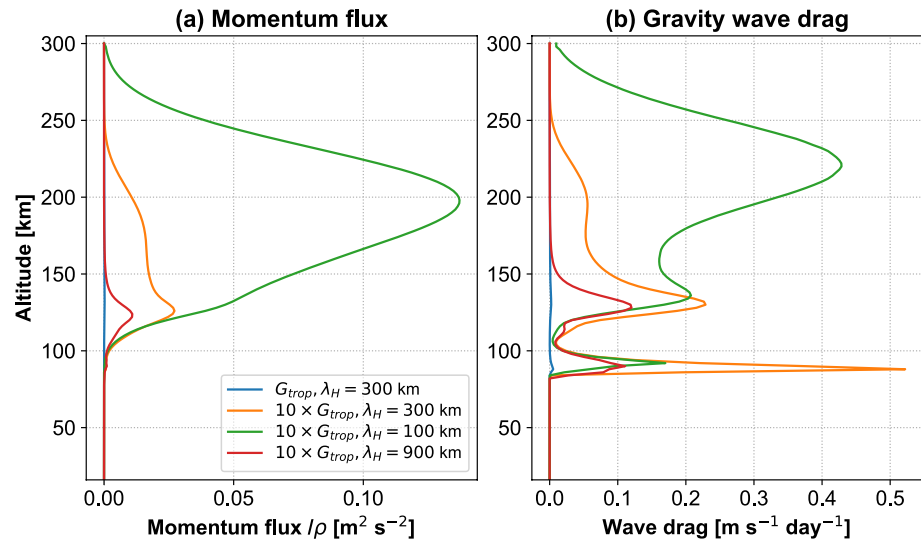
Figure 8. The calculated (a) momentum flux and (b) gravity wave drag produced by a localized source of secondary waves centered around 90 km, but without tropospheric sources. Blue lines are for the source intensity $G = G_{\text{trop}}$ and the characteristic horizontal wavelength $\lambda_H = 300$ km. The other experiments are for $G = 10 \times G_{\text{trop}}$ and λ_H as indicated in the legend.

$\lambda_H = 300$ km for $G = G_{\text{trop}}$ (blue lines), $G = 10 \times G_{\text{trop}}$ (orange) and $G = 100 \times G_{\text{trop}}$ (not shown). It is immediately seen that both momentum flux (left panel) and the associated GW drag (right panel) scale approximately as G^2, which also follows from Equation 18. Thus, the increase of the source strength by a factor 100 produces four orders of magnitude larger peak values $F_M \approx 2.7$ m^2 s^{-2} and $a \approx 22$ m s^{-1} d^{-1} (not plotted). However, a look at Figure 7 shows that these values represent approximately one-tenth of those accounting for tropospheric sources. In cases of $G = G_{\text{trop}}$ and $G = 10 \times G_{\text{trop}}$, the generated response in the thermosphere is, accordingly, four and two orders of magnitude smaller, that is, virtually negligible with respect to the effect produced by sources in the troposphere (Figure 7). In Section 7, we explain the choice of source magnitudes G selected for plotting.

The vertical wave damping by molecular diffusion and thermal conduction β_{mol} as well as that by ion friction β_{ion} (Equation 21) are both particularly strong in the thermosphere, and both are inversely proportional to the horizontal wavenumber of the harmonic. Figure 8 illustrates that the secondary harmonics with shorter horizontal scales experience less damping, propagate higher, grow to larger amplitudes, and produce stronger drag upon their ultimate dissipation. However, F_M and a do not scale with λ_H as clearly as with the source magnitude. The reason is that the attenuation of the flux also nonlinearly depends on the amplitude of the harmonic and of other components in the spectrum. Since the GW drag is determined by the shape of the $F_M(z)$ profile, therefore its dependence on the horizontal scale is more complex. Nevertheless, a thorough examination of Figure 8, in particular of the profiles calculated with the fixed source $G = 10 \times G_{\text{trop}}$ and $\lambda_H = 900$ (red), 300 (orange), and 100 km (green), shows that both the flux and drag decrease in rough proportion to decreasing k. To be more specific, the peak values of F_M in the thermosphere scale as $F_M(100\ \text{km}):F_M(300\ \text{km}):F_M(900\ \text{km}) \approx 5.1:1:0.4$. For the GW drag, these values are $a(100\ \text{km}):a(300\ \text{km}):a(900\ \text{km}) \approx 1.9:1:0.5$. We note that these peaks occur at different heights.

7. Discussion

7.1. Can GW Parameterizations Ignore Sources in the Middle Atmosphere?

The majority of parameterizations designed to capture effects of subgrid-scale GWs in GCMs place the sources in the troposphere or lowermost stratosphere. Although the numerical experiments of Ribstein et al. (2022) accounted for higher altitude sources, these sources apparently did not contribute noticeably to the mesospheric GW drag in their model. By assuming that the wave forcing is uniformly distributed in the middle atmosphere and that it is at most a factor of two stronger than that in the troposphere, Figure 5 in Section 4 demonstrated that the neglect of wave generation in the middle atmosphere may underestimate the drag above the mesopause by no more than a factor of two. Section 5 explored the effects of a range of localized middle atmosphere sources

combined with the benchmark tropospheric forcing. In order for these localized sources to produce significant extra drag in the thermosphere, they had to be considerably stronger than in the troposphere. The drag produced was found to be very sensitive to the source altitude, with higher launch altitudes requiring much stronger forcing. Both of these effects can be attributed to density rapidly decreasing with altitude.

In many GWD parameterizations, the characteristic horizontal wavelength λ_H commonly serves as a putative parameter to be tuned within a limited interval reflecting the subgrid nature of the waves, usually a few hundred kilometers. The results of Section 6 show that such uncertainty in λ_H produces a factor of few uncertainty in the magnitude of the calculated wave drag. This explains why the parameterizations accounting for only tropospheric sources can reproduce the bulk effect of GWs in models fairly well: they are tuned with λ_H to compensate for any missing or excessive drag. Sometimes, a so-called "intermittency factor", or a putative coefficient that scales the calculated drag, is imposed along with the tunable λ_H. Such an approach is probably justified in view of the lack of knowledge of GW generation in the entire atmosphere.

It is important to recognize that we assumed the most favorable conditions in our calculations, when the sources always act in sync and add maximum of the momentum to the harmonic originated in the troposphere ($\sin \phi = 1$ in Equation 18). This is unlikely the case in the real atmosphere: the phase shift ϕ can vary, and the sources in upper layers would not necessarily supply the maximum momentum to harmonics propagating from below and, at least in this model, could potentially attenuate them. Therefore, the net impact of the sources is smaller than the estimated here, and so the fact that their gross effect is missing in parameterizations is less significant. Even without considering particular forcing mechanisms, it is however clear that the contribution of secondary sources to the accumulated wave momentum must decrease with height following the density reduction.

7.2. How Important Are Secondary Waves?

Another notable inference from Section 6 concerning secondary GWs and their dynamical impact is the strong (quadratic) dependence on the magnitude of the forcing G. In the body forcing theory, it is based on the amount of momentum a transferred from primary harmonics (e.g., Vadas & Fritts, 2002, Equation 3). In our calculations presented in Figure 7c, the local peak of drag created by primary harmonics that dissipate just below the imposed localized source reaches $a \approx 150$ m s^{-1} d^{-1}, or ~$1.7 \cdot 10^{-3}$ m s^{-2}. For comparison, the sum of $|G_j|$ for the spectrum in Figure 1b gives the total tropospheric forcing $G_{\mathrm{trop}} \approx 3 \cdot 10^{-4}$ m s^{-2}. Thus, the forcing in the mesosphere due to primary wave dissipation is only about one order of magnitude stronger than that in the troposphere ($G \sim 10 \times G_{\mathrm{trop}}$), which explains our choice of sensitivity tests presented in Figure 8. Even if all of the momentum carried by dissipating primary harmonics was converted to secondary waves, comparing the orange and blue curves in Figure 7c shows that these secondary waves would generate only a small amount of extra drag in the thermosphere. Of course, assuming the momentum carried by primary harmonics is fully converted to secondary waves implies that primary waves impose no drag on the background flow. Obviously only a modest fraction of momentum carried by dissipating primary GWs can be transferred to secondary waves, and these in turn would generate an even smaller amount of additional drag in the thermosphere. The case with $G = G_{\mathrm{trop}}$, which represents about one-tenth of the momentum of the primary GWs (shown with the blue lines in Figure 8) demonstrates a very weak response in the thermosphere. A similar reasoning can be applied to nonlinear mechanism of secondary wave generation (Fritts et al., 2020, 2015).

8. Conclusions

We developed a framework for assessing a potential impact of GWs generated by sources distributed over all heights in the middle atmosphere. The sources are represented by a forcing term in the equation for horizontal momentum, whose values are expressed in terms of multiples of the forcing required to produce typical wave spectra just above the tropopause. This approach does not require a knowledge of specific generation mechanisms, but allows for evaluation of the relative importance of tropospheric and extra-tropospheric sources. For the purposes of this paper, the importance is defined in terms of the GW-induced vertical flux of horizontal momentum (momentum flux, for brevity) and the momentum transferred to the background flow, or GW drag. We performed a series of sensitivity calculations demonstrating the response in the thermosphere to the magnitude and location of extra-tropospheric sources. The main conclusions derived from this study are listed below.

1. Accumulation of wave momentum from vertically distributed sources steeply drops with height owing to the rapid decrease of density.

2. Forcing a representative tropospheric spectrum throughout the entire middle atmosphere at a rate that is twice that in the troposphere produces no more than a factor of two increase in thermospheric drag.

3. The neglect of extra-tropospheric sources in GW parameterizations commonly employed in GCMs can be (and probably is to some extent) compensated by tuning the characteristic horizontal wavelength, dissipation mechanisms and "intermittency factors" (in some schemes). All of these factors are uncertain to some degree.

4. Owing to the small density, localized forcing in the mesosphere must be unrealistically strong in order to produce momentum flux and drag in the thermosphere comparable to those produced by sources in the troposphere.

5. Assuming that wave forcing mechanisms are similar in all atmospheric layers, the impact of secondary waves must be negligible, that is, drag from primary GWs must prevail in the thermosphere.

We must emphasize that our estimates concern persistent GW effects, rather than individual occasional wave events. In this study, we assumed that sources across all heights act in sync to increase the momentum of the harmonic propagating from below. In the real atmosphere, this rarely occurs, therefore the results can be viewed as an upper limit estimate of the significance of secondary GWs. The real effect of extra-tropospheric sources should be smaller, but assessing it requires better quantification of GW sources and generation mechanism.

Our results have broader impact concerning the observed interpretation of upper atmosphere variability. Recent satellite measurements demonstrate that the horizontal winds exhibit a substantial degree of variability in direction and magnitude, which rapidly evolve as a function of altitude (Yiğit et al., 2022). The observed degree of wind variability cannot be explained considering only space weather processes. Characterization of the mean state and variability of the thermosphere-ionosphere system require accurately accounting for the effects of GWs of varying sources, especially of the ones originating in the lower atmosphere, as indicated by our numerical experiments. Overall, our framework provides a practical physics-based approach to the primary and secondary waves, continuously evaluating their interactions with the mean flow.

The developed framework is, effectively, an extension of the nonlinear spectral parameterization scheme of Medvedev and Klaassen (2000) and Yiğit et al. (2008) for capturing the effects of small-scale GWs in GCMs. Due to its sufficiently general formulation, the framework can readily be applied to studying particular generation mechanisms and GW sources. Further insight into the dynamical role of waves from different sources can be gained, once they are quantified.

The present column model does not include nonhydrostatic waves and therefore omits vertical trapping and back reflection of harmonics. However, these processes tend to reduce the momentum flux reaching the thermosphere, and therefore would not change the present conclusions. Consideration of two- and three-dimensional wave propagation would require more sophisticated numerical modeling. Such effects would account for dispersion and spreading of packets and other details of wave propagation that are important for considering individual wave events (e.g., Bölöni et al., 2021; Kim et al., 2021). However, such details cannot change our conclusions regarding the reduced effects of high-altitude sources owing to density stratification. Nor could such details change the fact that breaking primary waves exert a force on the background flow, so that secondary waves generated during wave breaking events are expected to transport significantly less momentum than the breaking primary waves that generated them.

Since we have adapted a particular GWD scheme for this study, it is natural to ask to what extent the results would differ if another scheme had been employed. While GW parameterizations do employ differing representations of wave breaking and sources, it should be recognized that all schemes capable of reproducing the zonally averaged circulation in the middle atmosphere share critical level effects and Doppler shifting by the background wind, two processes that are well-defined and known to be critical for reproducing the effects of GWs on the circulation of the middle atmosphere. We have explored a range of source strengths that should be sufficient to cover any differences between parameterizations, therefore our estimates for the effects of secondary waves in the thermosphere are considered to be robust.

Data Availability Statement

References

Bölöni, G., Kim, Y.-H., Borchert, S., & Achatz, U. (2021). Toward transient subgrid-scale gravity wave representation in atmospheric models. Part I: Propagation model including nondissipative wave-mean-flow interactions. *Journal of the Atmospheric Sciences*, *78*(4), 1317–1338. https://doi.org/10.1175/JAS-D-20-0065.1

Chun, H.-Y., & Kim, Y.-H. (2008). Secondary waves generated by breaking of convective gravity waves in the mesosphere and their influence in the wave momentum flux. *Journal of Geophysical Research*, *113*(D23), D23107. https://doi.org/10.1029/2008JD009792

Fritts, D. C., Dong, W., Lund, T. S., Wieland, S., & Laughman, B. (2020). Self-acceleration and instability of gravity wave packets: 3. Three-dimensional packet propagation, secondary gravity waves, momentum transport, and transient mean forcing in tidal winds. *Journal of Geophysical Research: Atmospheres*, *125*(3), e2019JD030692. https://doi.org/10.1029/2019JD030692

Fritts, D. C., Laughman, B., Lund, T. S., & Snively, J. B. (2015). Self-acceleration and instability of gravity wave packets: 1. Effects of temporal localization. *Journal of Geophysical Research: Atmospheres*, *120*(17), 8783–8803. https://doi.org/10.1002/2015JD023363

Fritts, D. C., Lund, A. C., Lund, T. S., & Yudin, V. (2022). Impacts of limited model resolution on the representation of mountain wave and secondary wave dynamics in local and global models: 2. Mountain wave and secondary wave evolutions in the thermosphere. *Journal of Geophysical Research: Atmospheres*, *127*(9), e2021JD036035. https://doi.org/10.1029/2021JD036035

Heale, C. J., Bossert, K., Vadas, S. L., Hoffmann, L., Dörnbrack, A., Stober, G., et al. (2020). Secondary gravity waves generated by breaking mountain waves over Europe. *Journal of Geophysical Research: Atmospheres*, *125*(5), e2019JD031662. https://doi.org/10.1029/2019JD031662

Heale, C. J., Inchin, P. A., & Snively, J. B. (2022). Primary versus secondary gravity wave responses at *F* region heights generated by a convective source. *Journal of Geophysical Research: Space Physics*, *127*(1), e2021JA029947. https://doi.org/10.1029/2021JA029947

Hertzog, A., Boccara, G., Vincent, R. A., Vial, F., & Cocquerez, P. (2008). Estimation of gravity wave momentum flux and phase speeds from quasi-Lagrangian stratospheric balloon flights. Part II: Results from the Vorcore campaign in Antarctica. *Journal of the Atmospheric Sciences*, *65*(10), 3056–3070. https://doi.org/10.1175/2008jas2710.1

Holton, J. R. (2004). *An introduction to dynamic meteorology* (4th ed.). Elsevier Academic Press.

Jones, W. L. (1967). Propagation of internal gravity waves in fluids with shear flow and rotation. *Journal of Fluid Mechanics*, *30*(3), 439–448. https://doi.org/10.1017/S0022112067001521

Kim, Y.-H., Bölöni, G., Borchert, S., Chun, H.-Y., & Achatz, U. (2021). Toward transient subgrid-scale gravity wave representation in atmospheric models. Part II: Wave intermittency simulated with convective sources. *Journal of the Atmospheric Sciences*, *78*(4), 1339–1357. https://doi.org/10.1175/JAS-D-20-0066.1

Kogure, M., Yue, J., Nakamura, T., Hoffmann, L., Vadas, S. L., Tomikawa, Y., et al. (2020). First direct observational evidence for secondary gravity waves generated by mountain waves over the Andes. *Geophysical Research Letters*, *47*(17), e2020GL088845. https://doi.org/10.1029/2020GL088845

Medvedev, A. S., & Klaassen, G. P. (1995). Vertical evolution of gravity wave spectra and the parameterization of associated wave drag. *Journal of Geophysical Research*, *100*(D12), 25841–25853. https://doi.org/10.1029/95JD02533

Medvedev, A. S., & Klaassen, G. P. (2000). Parameterization of gravity wave momentum deposition based on nonlinear wave interactions: Basic formulation and sensitivity tests. *Journal of Atmospheric and Solar-Terrestrial Physics*, *62*(11), 1015–1033. https://doi.org/10.1016/S1364-6826(00)00067-5

Medvedev, A. S., & Yiğit, E. (2019). Gravity waves in planetary atmospheres: Their effects and parameterization in global circulation models. *Atmosphere*, *10*(531), 531. https://doi.org/10.3390/atmos10090531

Miao, J., Gao, H., Kou, L., Zhang, Y., Li, Y., Chu, Z., et al. (2022). A case study of midlatitude noctilucent clouds and its relationship to the secondary-generation gravity waves over tropopause inversion layer. *Journal of Geophysical Research: Atmospheres*, *127*(17), e2022JD036912. https://doi.org/10.1029/2022JD036912

Miyoshi, Y., Fujiwara, H., Jin, H., & Shinagawa, H. (2014). A global view of gravity waves in the thermosphere simulated by a general circulation model. *Journal of Geophysical Research: Space Physics*, *119*(7), 5807–5820. https://doi.org/10.1002/2014JA019848

Otsuka, Y. (2021). Medium-scale traveling ionospheric disturbances. In *Ionosphere dynamics and applications* (pp. 421–437). American Geophysical Union (AGU). (Section: 18). https://doi.org/10.1002/9781119815617.ch18

Polyanin, A. D., & Zaitsev, V. F. (2017). *Handbook of ordinary differential equations: Exact solutions, methods, and problems* (3rd ed.). Taylor & Francis Inc. Retrieved from https://xn--webducation-dbb.com/wp-content/uploads/2019/04/Andrei-D.-Polyanin-Valentin-F.-Zaitsev-Handbook-of-Ordinary-Differential-Equations_-Exact-Solutions-Methods-and-Problems-Chapman-and-Hall_CRC-2018.pdf

Ribstein, B., Millet, C., Lott, F., & de la Cámara, A. (2022). Can we improve the realism of gravity wave parameterizations by imposing sources at all altitudes in the atmosphere? *Journal of Advances in Modeling Earth Systems*, *14*(2), e2021MS002563. https://doi.org/10.1029/2021MS002563

Vadas, S. L., & Fritts, D. C. (2002). The importance of spatial variability in the generation of secondary gravity waves from local body forces. *Geophysical Research Letters*, *29*(20), 451–454. https://doi.org/10.1029/2002GL015574

Vadas, S. L., Fritts, D. C., & Alexander, M. J. (2003). Mechanism for the generation of secondary waves in wave breaking regions. *Journal of the Atmospheric Sciences*, *60*(1), 194–214. https://doi.org/10.1175/1520-0469(2003)060⟨0194:MFTGOS⟩2.0.CO;2

Vadas, S. L., Zhao, J., Chu, X., & Becker, E. (2018). The excitation of secondary gravity waves from local body forces: Theory and observation. *Journal of Geophysical Research: Atmospheres*, *123*(17), 9296–9325. https://doi.org/10.1029/2017JD027970

Williams, P. J. S. (1989). Observations of atmospheric gravity waves with incoherent scatter radar. *Advances in Space Research*, *9*(5), 65–72. https://doi.org/10.1016/0273-1177(89)90342-6

Yiğit, E., Aylward, A. D., & Medvedev, A. S. (2008). Parameterization of the effects of vertically propagating gravity waves for thermosphere general circulation models: Sensitivity study. *Journal of Geophysical Research*, *113*(D19), D19106. https://doi.org/10.1029/2008JD010135

Yiğit, E., Dhadly, M., Medvedev, A. S., Harding, B. J., Englert, C. R., Wu, Q., & Immel, T. J. (2022). Characterization of the thermospheric mean winds and circulation during solstice using ICON/MIGHTI observations. *Journal of Geophysical Research: Space Physics*, *127*(11), e2022JA030851. https://doi.org/10.1029/2022JA030851

Yiğit, E., & Medvedev, A. S. (2010). Internal gravity waves in the thermosphere during low and high solar activity: Simulation study. *Journal of Geophysical Research*, *115*(A8). https://doi.org/10.1029/2009JA015106

Yiğit, E., & Medvedev, A. S. (2013). Extending the parameterization of gravity waves into the thermosphere and modeling their effects. In F.-J. Lübken (Ed.), *Climate and Weather of the Sun-Earth System (CAWSES)* (pp. 467–480). Springer Netherlands. https://doi.org/10.1007/978-94-007-4348-9_25

Yiğit, E., & Medvedev, A. S. (2015). Internal wave coupling processes in Earth's atmosphere. *Advances in Space Research*, *55*(5), 983–1003. https://doi.org/10.1016/j.asr.2014.11.020

Yiğit, E., & Medvedev, A. S. (2019). Obscure waves in planetary atmospheres. *Physics Today*, *72*(6), 40–46. https://doi.org/10.1063/PT.3.4226

Yiğit, E., Medvedev, A. S., Aylward, A. D., Hartogh, P., & Harris, M. J. (2009). Modeling the effects of gravity wave momentum deposition on the general circulation above the turbopause. *Journal of Geophysical Research*, *114*(D7), D07101. https://doi.org/10.1029/2008JD011132

Yiğit, E., Medvedev, A. S., Aylward, A. D., Ridley, A. J., Harris, M. J., Moldwin, M. B., & Hartogh, P. (2012). Dynamical effects of internal gravity waves in the equinoctial thermosphere. *Journal of Atmospheric and Solar-Terrestrial Physics*, *90–91*, 104–116. https://doi.org/10.1016/j.jastp.2011.11.014

Yiğit, E., Ridley, A. J., & Moldwin, M. B. (2012). Importance of capturing heliospheric variability for studies of thermospheric vertical winds. *Journal of Geophysical Research: Space Physics*, *117*(A7). https://doi.org/10.1029/2012JA017596